JOURNAL OF COMPUTATIONAL PHYSICS 110, 274–284 (1994)

Liquid–Liquid Driven Cavity Flow

G. MANSELL, J. WALTER, AND E. MARSCHALL

Department of Mechanical and Environmental Engineering, University of California, Santa Barbara, Santa Barbara, California 93106

Received July 13, 1992

Liquid–liquid driven cavity flow was studied numerically. Information on "realistic" liquid–liquid interface conditions were obtained from photochromic flow visualization experiments. With this input, numerically obtained flow fields agreed well with experimentally observed flow fields. A parametric numerical study showed the influence of various parameters on the behavior of interface velocity and tangential shear stress gradients in the vicinity of the liquid–liquid interface.

1. INTRODUCTION

Driven cavity flow has been used frequently for testing and evaluating numerical techniques. Usually, the case considered involves a square cavity which is filled with a fluid. The top wall moves with a uniform velocity in its own plane. Movements inside the cavity are caused by the tangential shear stress to which the fluid is subjected by the moving top wall. Solutions for laminar flow in a driven cavity over a wide range of Reynolds numbers have been presented by various authors [1–5].

The problem considered in this study involves two immiscible liquids. One liquid is confined in a square cavity, while the second, lighther liquid flows across the top of the cavity. Isothermal conditions are assumed; therefore, all movements of the fluid within the cavity are caused by the lighter fluid flowing across the cavity.

The mathematical description of the liquid–liquid driven cavity problem is straightforward, with the exception of the description of the liquid–liquid interface. The physical characteristics of liquid–liquid interfaces have been discussed for nearly one century. A widely held view states that the liquid–liquid interface characteristics depend strongly on interface tension gradients and that the interface tension gradients depend strongly on concentration gradients of surface-active contaminants. This subject has been discussed extensively by Scriven [6], Harper [7], Frumkin and Levich [8, 9], Savic [10], Griffith [11], Davis and Acrivos [12], Levich [13], and many others. Interface tension gradients tend to reduce the mobility of a liquid–liquid interface. If an interface is fully mobile, it is characterized by continuous tangential shear stress across the interface. If an interface is not fully mobile or even rigid, tangential shear stresses on both sides of the interface take on different values. Since totally mobile interfaces have rarely been observed, one must either conclude that the surface contamination is not the only reason for the reduced mobility of the liquid–liquid interfaces or one must conclude that surface active substances are virtually always present. Since the degree of contamination of industrial grade fluids is usually unknown and cannot easily be determined, the prediction of interface characteristics is difficult to make. In order to overcome this obstacle, a series of experiments was carried out, providing sufficient information for a "realistic" interface description.

2. EXPERIMENTS

A detailed description of the experimental apparatus used in this study was provided by Walter [15]. An essential part of the experimental setup was a horizontal flow channel which was 25.4 mm wide and 10.2 mm high. A rectangular cavity was provided at the bottom of the channel. The cavity was 25.4 mm wide and 9 mm deep. Its length could be varied from 0 to 20 mm. The cavity was located 1.1 m from the channel entrance. The walls of the cavity and the adjacent flow channel were made from plexiglass. A glass window was provided at the bottom of the cavity to allow determination of flow fields in the cavity and the channel with the help of a flow visualization technique.

The cavity was filled with a mixture of ethanol and water while a laminar flow of a petroleum solvent known as AMSCO mineral spirits was maintained in the channel. The ethanol–water mixture and the petroleum solvent did not mix and showed a clearly identifiable interface. Channel fluid and cavity fluid contained radiachromic dyes. These dyes, hexahydroxyethyl pararosaniline cynide dissolved in the water–ethanol mixture and the photochromic dye

0021-9991/94 $6.00

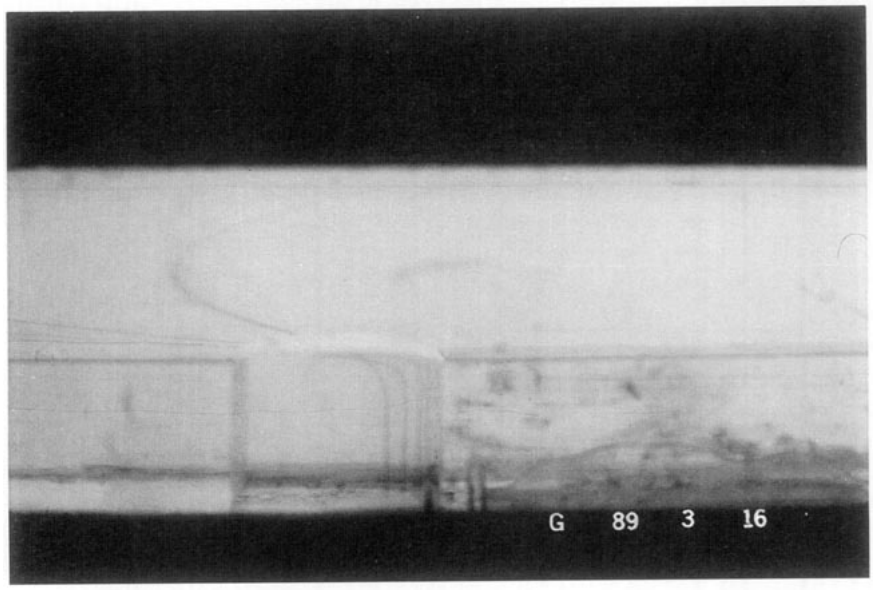

FIG. 1. Liquid–liquid driven cavity flow.

1′,3′,3-trimethyl-6′-nitroindoline-2-spiro-2-2′-benzopyran dissolved in the petroleum solvent, are colorless in the absence of ultraviolet light. They can be readily activated with a nitrogen pulse laser to produce well-defined narrow colored lines in the fluid. The movement of these originally straight lines may be either simply observed to obtain a qualitative impression of the flow or they may be recorded with high speed photography for later evaluation. Details of this flow visualization technique have been discussed elsewhere [16, 17].

Figure 1 shows the cavity at the bottom of the flow channel. Also seen are dye traces which were produced by laser pulses. The laser beams were directed across the window at the bottom of the cavity so as to produce straight dye traces perpendicular to the channel flow. The laser was also moved from right to left in order to create each trace in a different location in the cavity. Therefore, the trace on the left in the cavity corresponds to the trace on the right in the channel flow. As can be seen, the flow is quite weak in the cavity and it is quite strong in the flow channel, even though the viscosities of the immiscible fluids were of the same order of magnitude.

Each laser pulse activated a dye trace in the cavity and channel flow. High speed movies were made of the movements and distortion of these traces: Sequential frames of the high speed movie were used to obtain velocity information. In general, one frame was selected which showed a trace immediately after activation. At that time, the trace was virtually vertical and straight as is indicated in Fig. 2. A second frame was selected which showed some movement and distortion of that trace. The time was known during which this movement and distortion took place, since the movies were taken at a known speed, usually 400 frames per second. It was necessary to determine the exact position of points located on the traces, so that quantitative velocity information could be obtained. This was done with help of an x-y-digitizer linked to a computer. Details of the procedure were discussed by Walter. The results of the procedure included information on interface velocities, tangential shear stress on both sides of the interface, and influence of flow rates and geometry of the cavity on the interface characteristics.

In particular it was found that the shear stresses at both sides of the liquid–liquid interface were not equal in all the cases tested. It was also found, that except near the edges of the cavity, the difference in shear stress on both sides of the liquid–liquid interface did not depend on the interface location. Scriven [6] presented a completely general formulation of the dynamics of a Newtonian fluid interface. In his formulation, the rheological behavior of the interface is characterized by its interfacial tension and surface viscosity. A result of his studies was that, for a two-dimensional flow,

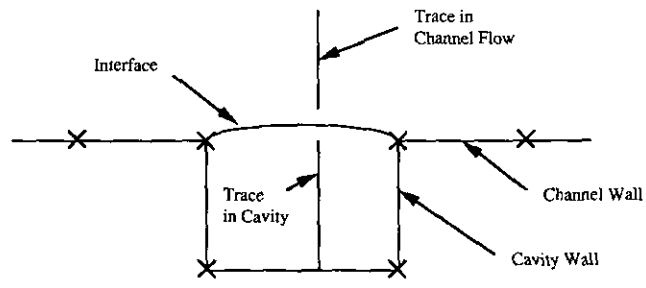

FIG. 2. Schematic of cavity image.

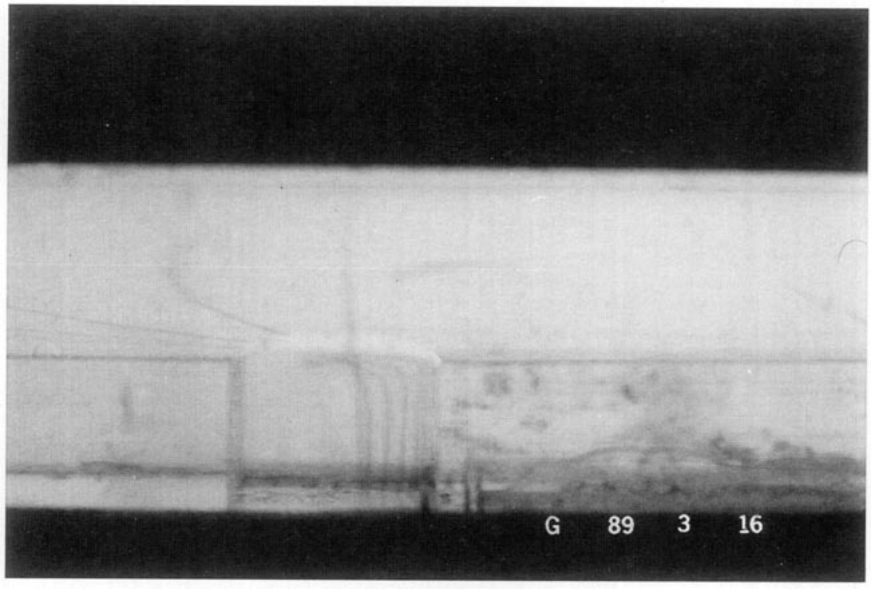

FIG. 3. Liquid–liquid driven cavity flow, mobile interface.

the difference in shear stress on both sides of a plane liquid–liquid interface is given by the relationship

$$\Delta\tau = \frac{\partial\sigma}{\partial y} + (\kappa + \varepsilon)\frac{\partial^2 W}{\partial y^2}, \tag{1}$$

where y is the coordinate aligned with the surface, κ and ε represent coefficients of surface viscosity, W is the tangential velocity of either phase at the interface, and σ is the surface (or interface) tension. Given a constant or nearly constant interface velocity over most of the length of the cavity, one must conclude that the interface tension σ varied linearly with the cavity length if Eq. (1) is correct. Other observations included:

(a) The ratio of shear stress at the cavity side to the shear stress at the channel side is small (much less than one) for low bulk flow velocities. This ratio is increasing (approaching one) with increasing bulk flow velocities. Therefore, it may be concluded that the interface is becoming more mobile as the bulk flow velocity increases.

(b) The ratio of cavity shear stress to channel shear stress is increasing with cavity length and approach values of the order of one. Interfaces of long cavities are more mobile than interfaces of short cavities. This can be clearly seen in Figs. 3 and 4.

(c) Increasing the length of the cavity increased the interface velocity.

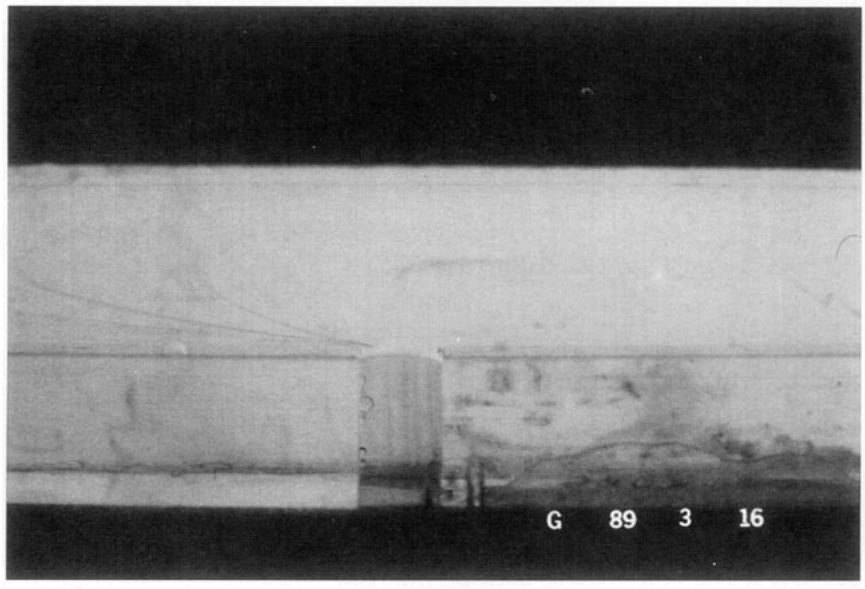

FIG. 4. Liquid–liquid driven cavity flow, rigid interface.

These observations are not unexpected, and they agree with observations made on liquid drops falling or rising in a second, immiscible liquid [14].

2. NUMERICAL STUDY

The flow in a liquid–liquid driven cavity was simulated numerically using a modified marker-and-cell (MAC) finite difference scheme. The specific flow and geometric parameters of the experimental study were used in order to assess the applicability of the numerical results. Through variation of the channel–cavity geometry, as well as the fluid properties and flow velocities, the qualitative results of the numerical simulation were examined and compared to those of experiment.

Mathematical Formulation

The geometry of the channel–cavity configuration is shown in Fig. 5. Here a Cartesian coordinate system is situated with the origin at the lower left-hand corner of the solution domain. A cavity of length L_{cav} and height H is located a distance X_{cav} from the origin in the lower wall of a channel of height C. Fluid of density ρ_c and viscosity μ_c fills the cavity, while fluid of density ρ_f and viscosity μ_f flows continuously into the channel from the left and exits on the right. The interface between the two immiscible fluids is characterized by the interface tension coefficient σ, and gravity acts in the negative y-direction. All solid boundaries are assumed to be rigid no-slip walls and the inlet and outlet of the channel are considered continuative inflow and outflow boundaries, respectively.

In addition, the following assumptions are made:

(a) The flow is laminar and two-dimensional. Three-dimensional effects can be minimized by assuming a large enough cavity width to length ratio. Since transition to turbulence for fully developed channel flow occurs at Reynold's numbers on the order of 2000, laminar flow can be maintained if the flow rate in the channel does not exceed a value consistent with an appropriate critical Reynold's number.

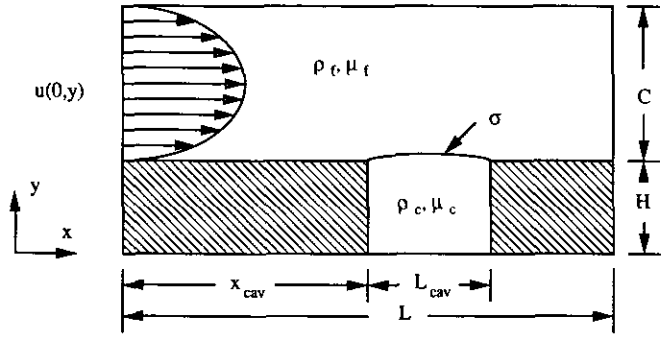

FIG. 5. Channel–cavity geometry and nomenclature.

(b) The fluids are Newtonian and characterized by constant thermophysical properties. For the bulk fluids, there is no reason to expect non-Newtonian fluid behavior, but for the fluid near the material interface there are various theories concerning the appropriate stress–strain relationship [6, 18]. The assumption of constant physical properties is reasonable since no temperature or concentration gradients are considered.

(c) The problem is isothermal. With this assumption, any free-convection effects can be neglected.

(d) In the presence of surfactants, the concentration of surfactant species in the interfacial fluid region will vary, and it is assumed that this variation is such as to cause a linear variation in the value of the interfacial tension coefficient. It is this assumption which resulted from the experiments.

Governing Equations

The governing equations are the familar 2D Navier–Stokes equations of fluid motion,

$$\frac{\partial u}{\partial t}+u\frac{\partial u}{\partial x}+v\frac{\partial u}{\partial t}=-\frac{1}{\rho}\frac{\partial p}{\partial x}+g_x+\nu\left(\frac{\partial^2 u}{\partial x^2}+\frac{\partial^2 u}{\partial y^2}\right) \quad (2)$$

$$\frac{\partial v}{\partial t}+u\frac{\partial v}{\partial x}+v\frac{\partial v}{\partial t}=-\frac{1}{\rho}\frac{\partial p}{\partial y}+g_y+\nu\left(\frac{\partial^2 v}{\partial x^2}+\frac{\partial^2 v}{\partial y^2}\right), \quad (3)$$

together with the equation of continuity,

$$\frac{\partial u}{\partial x}+\frac{\partial v}{\partial y}=0. \quad (4)$$

Here, velocity components (u, v) are in the Cartesian coordinate directions (x, y), (g_x, g_y) denote body accelerations, ν is the kinematic viscosity, ρ is the fluid density, and p is the fluid pressure.

As a means of incorporating the pressure and the condition of incompressibility into the numerical solution algorithm, we allow for limited compressibility effects [19] and rewrite Eq. (4) as

$$\frac{1}{\rho c^2}\frac{\partial p}{\partial t}+\frac{\partial u}{\partial x}+\frac{\partial v}{\partial y}=0, \quad (5)$$

where c is the adiabatic speed of sound in the fluid.

Discrete finite difference approximations to Eqs. (2)–(5) are obtained through the use of a method originally proposed by Hirt and Nichols [20] which incorporates a volume of fluid function, F, in order to track material interfaces within the solution domain. Essentially, F is a step function, equal to unity for full computational cells containing fluid of density ρ_f and viscosity μ_f, and is equal to zero for full cells containing fluid of density ρ_c and viscosity μ_c.

Fractional values of F then indicate cells containing a material interface. The computational details involved in tracking the interface using the volume of fluid function may be found elsewhere [20, 21].

Locating the discrete values of the dependent variables at the cell positions shown in Fig. 6 results in the approximations to Eqs. (2) and (3),

$$u^{n+1}_{i+1/2,j} = u^n_{i+1/2,j} + \delta t[-(p^{n+1}_{i+1,j} - p^{n+1}_{i,j})/\delta\rho x_{i+1/2} + g_x - FUX - FUY + VISX] \quad (6)$$

$$v^{n+1}_{i,j+1/2} = v^n_{i,j+1/2} + \delta t[-(p^{n+1}_{i,j+1} - p^{n+1}_{i,j})/\delta\rho y_{j+1/2} + g_y - FVX - FVY + VISY], \quad (7)$$

where

$$\delta\rho x_{i+1/2} = \tfrac{1}{2}[(\rho_c + (\rho_f - \rho_c)\, F_{i,j})\, \delta x_{i+1} + (\rho_c + (\rho_f - \rho_c)\, F_{i+1,j})\, \delta x_i]$$

and

$$\delta\rho y_{j+1/2} = \tfrac{1}{2}[(\rho_c + (\rho_f - \rho_c)\, F_{i,j})\, \delta y_{j+1} + (\rho_c + (\rho_f - \rho_c)\, F_{i,j+1})\, \delta y_j].$$

Here, for example, $p^{n+1}_{i,j}$ represents the value of $p(x, y, t)$ at time $(n+1)\,\delta t$ and at a location centered in the ith cell in the x-direction and the jth cell in the y-direction. Half integer subscripts refer to cell boundary locations. Also, $\delta x_{i+1/2} = \frac{1}{2}(\delta x_i + \delta x_{i+1})$ and $\delta y_{j+1/2} = \frac{1}{2}(\delta y_j + \delta y_{j+1})$, FUX is the advective flux of u in the x-direction, FUY is the advective flux of u in the y-direction, $VISX$ is the viscous acceleration in the x-direction and similarly for the y-direction advective and viscous acceleration terms. All these terms are evaluated using the old time-level (n) values for velocities.

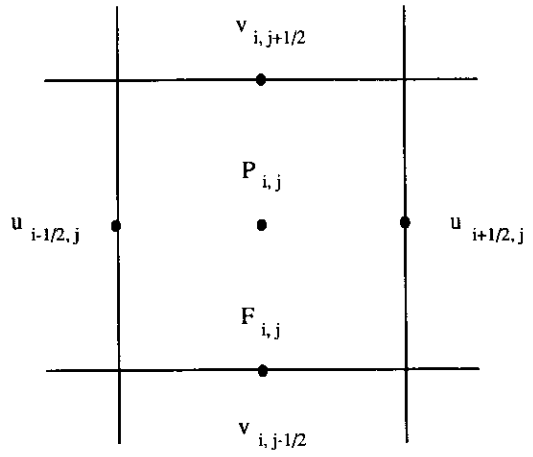

FIG. 6. Location of variables in the MAC computational cell.

Evaluation of the advective flux terms requires special care to ensure conservation of momentum on a variable mesh while maintaining both accuracy and stability of the numerical solution as discussed in [20]. Thus, a combined central difference-donor cell approximation is used for the advective flux terms as

$$FUX = \frac{u_{i+1/2,j}}{\delta x_\alpha}[\delta x_{i+1} DUL + \delta x_i DUR + \alpha\, \mathrm{sgn}(u)(\delta x_{i+1} DUL - \delta x_i DUR)],$$

where

$$DUL = (u_{i+1/2,j} - u_{i-1/2,j})/\delta x_i;$$

$$DUR = (u_{i+3/2,j} - u_{i+1/2,j})/\delta x_{i+1};$$

$$\delta x_\alpha = \delta x_{i+1} + \delta x_i + \alpha\, \mathrm{sgn}(u)(\delta x_{i+1} - \delta x_i)$$

and $\mathrm{sgn}(u)$ means the sign of $u_{i+1,j}$. The parameter α controls the amount of donor cell differencing used in the approximation. Analogous expressions are used for FUY, FVX, and FVY. All viscous acceleration terms are approximated with standard centered differences.

Boundary Conditions

Referring to Fig. 5, the applicable boundary conditions for the bulk fluids can be stated as

$$\begin{aligned}
u = 0;\ v = 0 \qquad & y = H;\ 0 \leqslant x \leqslant x_{cav};\ x \geqslant x_{cav} + L_{cav} \\
u = 0;\ v = 0 \qquad & y = 0;\ x_{cav} \leqslant x \leqslant x_{cav} + L_{cav} \\
u = 0;\ v = 0 \qquad & y = H + C;\ x \geqslant 0 \\
u = 0;\ v = 0 \qquad & x = x_{cav};\ 0 \leqslant y \leqslant H \\
u = 0;\ v = 0 \qquad & x = x_{cav} + L_{cav};\ 0 \leqslant y \leqslant H \\
u = f(y);\ v = 0 \qquad & x = 0;\ y \geqslant H \\
\frac{\partial u}{\partial x} = 0;\ \frac{\partial v}{\partial x} = 0 \qquad & x = L,\ y > H,
\end{aligned}$$

where $f(y)$ is the velocity profile of Poiseuille flow.

The preceding boundary conditions are enforced in the numerical scheme through use of a layer of fictitious cells surrounding the computational mesh as discussed by Mansell [21] and Welch *et al.* [22].

The Material Interface

For the numerical study we restrict attention to a nearly plane two-dimensional interface so that Eq. (1) is applicable. The last term on the right-hand side of Eq. (1) represents the viscous shearing stress due to the stretching or contraction of the interfacial monolayer between the two

fluids. Numerical estimates indicate that, except near the ends of the cavity where the interface must decelerate rapidly in order to satisfy the boundary conditions at the cavity walls, the value of d^2W/dy^2 is several orders of magnitude smaller than the interfacial tension gradient for the cases considered here. In addition, results of the experimental study have shown that the interface velocity is nearly independent of position along the interface. Therefore, this term will be neglected here and only the influence of an interfacial tension gradient will be considered. Thus, we rewrite Eq. (1) as

$$\tau_{cav} - \tau_{chan} \cong \frac{\partial \sigma}{\partial l}, \tag{8}$$

where l is the coordinate aligned with the material surface. For the numerical solution, we therefore assume that this is the appropriate dynamical condition to be applied at the boundary between the two bulk fluids.

Equation (8) is reformulated in terms of the tangential velocities near the interface. From the assumption of Newtonian fluid behavior and considering for the present time that the interface is nearly horizontal, we can express the tangential shear stresses at the interface in terms of the horizontal velocity components as

$$\left(\mu \frac{\partial u}{\partial y}\right)_c - \left(\mu \frac{\partial u}{\partial y}\right)_f = \frac{\partial \sigma}{\partial l}. \tag{9}$$

Referring to Fig. 7 and noting that the flow in the channel above the interface "drives" the flow in the cavity below, it is apparent that we must apply Eq. (9) in such a manner as

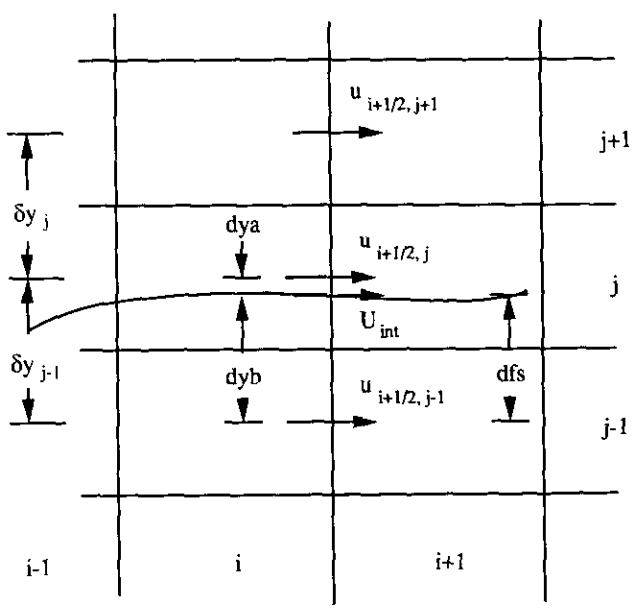

FIG. 7. Cell arrangement for applying interface stress conditions.

to relate the tangential velocities above the interface to the shear stress, and hence tangential velocities, below the interface.

Approximating the velocity gradients with finite differences we have

$$\left(\frac{\partial u}{\partial y}\right)_c = \left[\frac{U_{int} - u_{i+1/2,j-1}}{dyb}\right]; \qquad \left(\frac{\partial u}{\partial y}\right)_f = \left[\frac{u_{i+1/2,j} - U_{int}}{dya}\right]$$

where U_{int} is the tangential velocity at the interface, dya is the distance between the center of cell (i,j) and the interface, and dyb is the distance between the interface and the center of cell $(i,j-1)$. To obtain a value for U_{int} the horizontal velocity components above the interface are extrapolated as

$$U_{int} = u_{i+1/2,j} - \frac{(u_{i+1/2,j+1/2} - u_{i+1/2,j})}{\delta y_j} dya. \tag{10}$$

Combining Eq. (10) with the discretized representations for the velocity gradients in accordance with Eq. (9) we finally obtain a relation for $u_{i,j-1}$ that is consistent with the dynamic interfacial boundary condition, Eq. (14),

$$u_{i+1/2,j-1} = u_{i+1/2,j}\left(1 + \frac{dya}{\delta y_j} + \frac{\mu_f}{\mu_c}\frac{dyb}{\delta y_j}\right) - u_{i+1/2,j+1}\left(\frac{dya}{\delta y_j} + \frac{\mu_f}{\mu_c}\frac{dyb}{\delta y_j}\right) - \frac{dyb}{\mu_c}\left(\frac{\partial \sigma}{\partial l}\right)_{i+1/2,j} \tag{11}$$

In Eq. (11) above, it is assumed that the interfacial tension gradient $(\partial\sigma/\partial l)_{i+1/2,j}$ is constant along the interface, reflecting the assumption that the interfacial tension coefficient varies linearly due to the surfactant concentration gradient along the interface. Quantitatively, the variation of surfactant concentration is not considered explicitly in the present numerical model, but we assume qualitatively that it is such as to produce a linear variation of the surface tension coefficient.

The above approximation equations require knowledge of the material interface location within the computational surface cells. The method of determining the location of the interface based on the distribution of the volume of fluid function, F, is described in [20], and its implementation in the present context is discussed in [21].

The calculation of surface tension forces was considered, and a method of applying these forces as additional accelerations in the momentum equations was discussed by Daly [23]. For the case of a non-zero surface tension gradient a modification must be made. In this case, the interface tension coefficient varies along the interface; therefore the surface pressure used in defining these surface

tension forces also varies. For a constant interfacial tension coefficient, the surface pressure is given by

$$p_s = -\sigma K_{xy}, \tag{12}$$

where K_{xy} is the local curvature of the interface defined as the reciprocal of the principal radius of curvature in the x-y plane. If σ varies along the interface in the downstream direction, then Eq. (12) above must be replaced with

$$p_s(l) = -\sigma(l)\, K_{xy}, \tag{13}$$

where l is the distance along the interface. Now, assuming the interface deviates only slightly from the horizontal, we have as a first approximation

$$\frac{\partial \sigma}{\partial l} \cong \frac{\partial \sigma}{\partial x^*},$$

where x^* is measured from the leading edge of the cavity, i.e.,

$$x^* = x - x_{\text{cav}}$$

and

$$0 \leqslant x^* \leqslant L_{\text{cav}} - x_{\text{cav}}.$$

Letting σ_0 be the constant equilibrium value for a surfactant-free interface, we have

$$\sigma(x^*) = \sigma_0 + x^* \frac{\partial \sigma}{\partial x^*}. \tag{14}$$

For most Newtonian fluids and common surfactants, the interfacial tension coefficient decreases with increasing surfactant concentration, so $(\partial\sigma/\partial x^*) < 0$ and Eq. (14) expresses the fact that σ decreases linearly from a maximum value of σ_0 at the upstream portion of the interface. Equation (14) is then used to evaluate $p_s(l)$ in Eq. (13) and, finally, the proper interface tension forces for each interface cell in the computational mesh.

Numerical Results and Discussion

For the numerical simulation, the fluid properties of the experimental study were used. For the denser phase, an ethanol–water mixture, the density and kinematic viscosity were 0.915 g/cm^3 and 0.03068 cm^2/s, respectively, while the lighter phase in the channel, an AMSCO mineral oil, had a density of 0.755 g/cm^3 and kinematic viscosity of 0.02036 cm^2/s. While measurements of interfacial tension coefficients are difficult at best, due to the relatively high sensitivity to temperature and surfactant concentration gradients, Walter [15] reports a nominal value of 8.00 dynes/cm. Simulations were run for a maximum bulk flow velocity in the channel of $U_{\max} = 5.00$ and 10.00 cm/s for cavity aspect ratios, L_{cav}/H, of 0.50, 0.75, and 1.00.

Normalized values of the interface velocity at the centerline of the cavity were calculated and plotted along with experimentally obtained values for each of the cases considered. Figure 8 displays results for a channel centerline velocity of 10.00 cm/s. Two sets of numerically obtained data points are shown, one for $d\sigma/dx^* = 0.0$ and one for a non-zero interfacial tension gradient. Initially, since many researchers assume continuity of tangential shear stress across a material interface, it was assumed that $d\sigma/dx^*$ was identically zero. In this case, the situation corresponds to a completely mobile interface. Examination of Fig. 8 reveals that this assumption results in interface velocities approximately 200% higher, on average, than those obtained experimentally. Since any real system will involve some degree of contamination, it is reasonable to expect that the presence of surfactants will have a significant influence on the resulting flow fields and, therefore, must be considered.

For this reason, additional simulations were performed for non-zero values of the interfacial tension gradient, $d\sigma/dx^*$. It was found that for a given constant value of $d\sigma/dx^*$ the numerical simulation produced results comparable to those of experiment. The second set of data points in Fig. 8 illustrate these results for a value of $d\sigma/dx^*$ of -0.4 dynes/cm^2. As can be seen, the numerical and experimental results compare quite favorably. Based on these comparisons, it was concluded that the numerical model provides reasonable results for the assumed variation in σ.

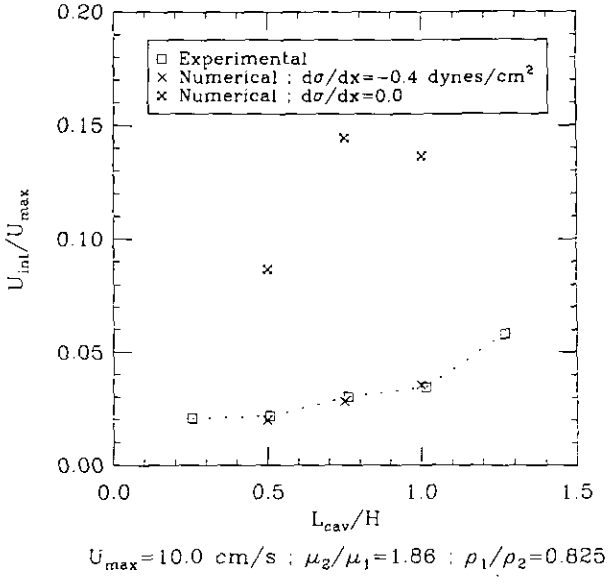

FIG. 8. Comparison of numerical and experimental results for the interface velocity.

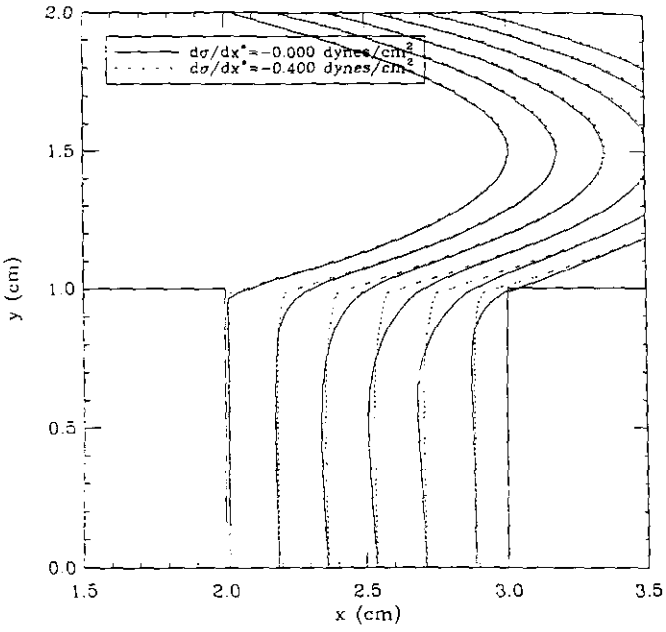

U_{max}=10.0 cm/s ; μ_2/μ_1=1.86 ; ρ_1/ρ_2=0.825 ; H/L_{cav}=1.00

FIG. 9. Normalized velocity profiles with and without interface tension gradients.

In Fig. 9 normalized horizontal velocity profiles through the cavity region of the flow field are displayed, while Fig. 10 and Fig. 11 display vector velocity plots for the test cases with $U_{max} = 10.00$ cm/s and a cavity aspect ratio of 1.00 for both zero and non-zero values of $d\sigma/dx^*$. The flow fields resulting from a non-zero surface tension gradient more closely resemble those of experiment.

Having deemed the numerical formulation acceptable through comparison with experimental results, a parametric

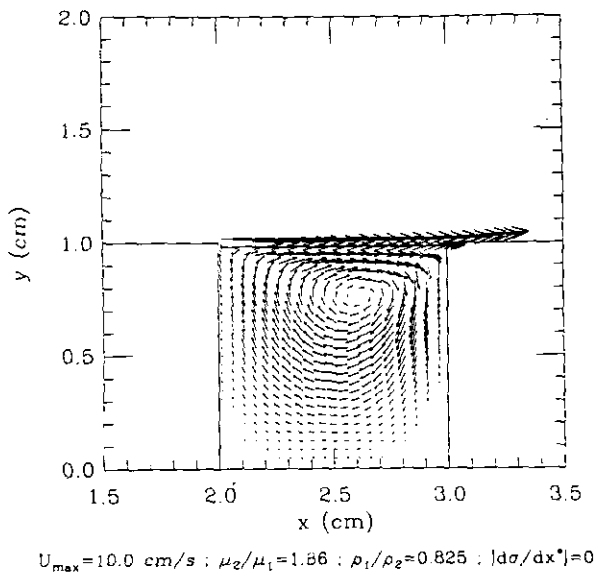

U_{max}=10.0 cm/s ; μ_2/μ_1=1.86 ; ρ_1/ρ_2=0.825 ; $|d\sigma/dx^*|$=0.000

FIG. 10. Vector plot of cavity flow.

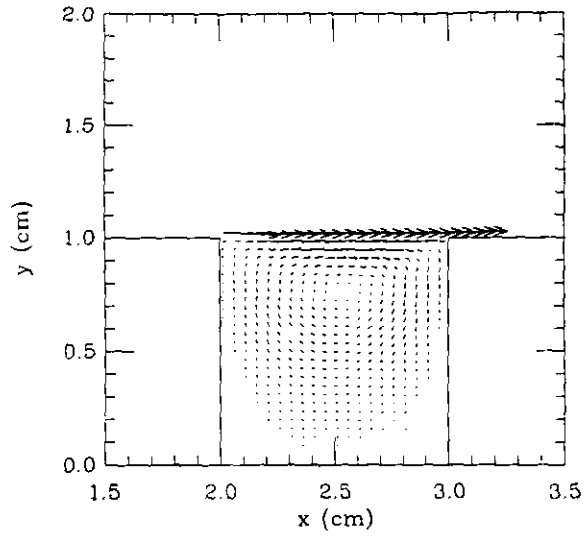

U_{max}=10.0 cm/s ; μ_2/μ_1=1.86 ; ρ_1/ρ_2=0.825 ; $|d\sigma/dx^*|$=0.400

FIG. 11. Vector plot of cavity flow.

study of the liquid–liquid driven-cavity problem was undertaken with specific emphasis directed towards the behavior of the velocity and tangential shear stress gradients in the vicinity of the material interface. Several simulations were performed for various fluid property ratios, channel–cavity configurations and bulk flow velocities in the channel. To limit the number of parameters involved, the densities of the two phases were kept constant at the following values; $\rho_1 = 0.75$ g/cm^3 for the lighter phase in the channel and $\rho_2 = 1.00$ g/cm^3 for the fluid in the cavity. The viscosity of the lighter phase was also held constant at $\mu_1 = 0.01$ cm^2/s, as was the maximum value of the interfacial tension coefficient at $\sigma_0 = 1.00$ dynes/cm. In addition, the height of the channel and the depth of the cavity were kept constant and equal as the length of the cavity was varied from 0.25 to 1.00 cm.

Finally, all cases were run on a variable mesh of 102×102 cells with dimensions of $\delta x_{min} = 0.025$ cm, $\delta y_{min} = 0.01875$ cm and $\delta x_{max} = 0.050$ cm, $\delta y_{max} = 0.025$ cm. To achieve adequate spatial resolution, the smallest dimensioned cells were located in the cavity region of the solution domain as well as extending partly into the channel in the vicinity of the interface. This situation proved to be sufficient in terms of accuracy and numerical stability considerations while still minimizing computer storage requirements.

Through variation of the kinematic viscosity of the denser fluid in the cavity, a range of dynamic viscosity ratios, μ_2/μ_1, from 1.5 to 5.33 was achieved. The maximum value of the interfacial tension coefficient, σ_0, was held constant at 1.00 dyne/cm while its spatial gradient in the flow direction was varied from zero, representing equality of shear stress at either side of the interface, to a maximum value correspond-

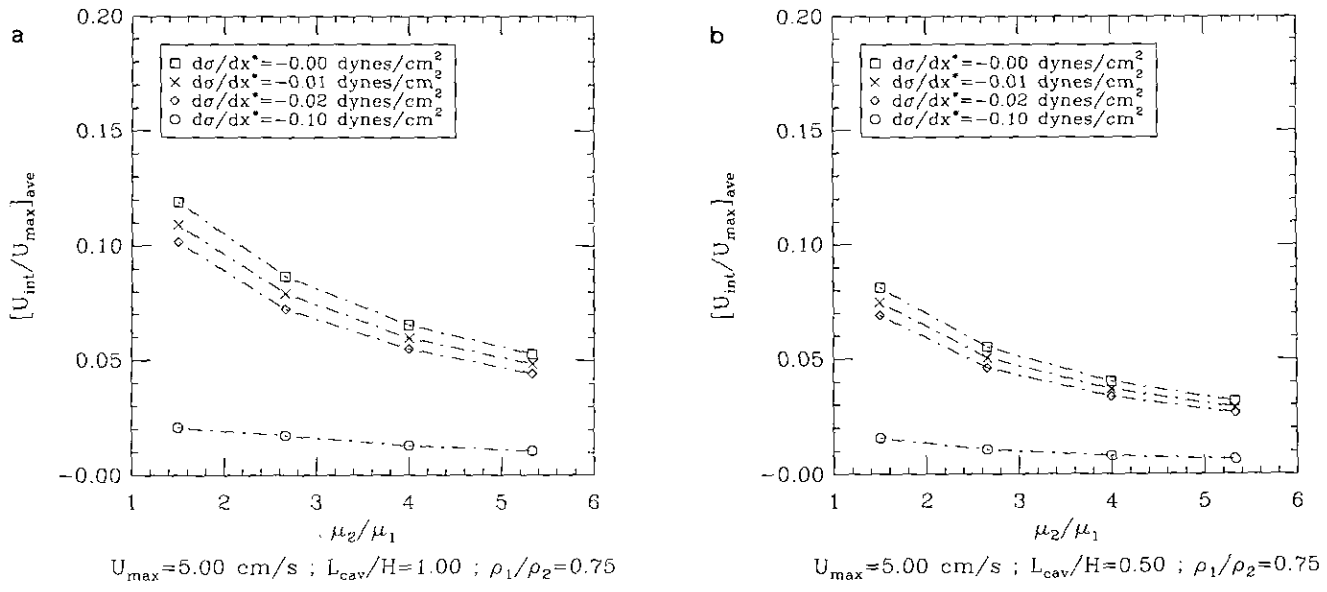

FIG. 12. Normalized interface velocity versus viscosity ratio.

ing to a 10% decrease at the downstream portion of the interface, resulting in a situation of negligible flow in the cavity for large cavity aspect ratios. Finally, all cases were run for channel centerline velocities of 1.00 and 5.00 cm/s. For a more extensive presentation of the numerical simulation results, the reader is referred to Ref. [21].

Figure 12 displays the influence of the dynamic viscosity ratio on the interface velocity for various values of the interfacial tension gradient, while Fig. 13 shows the corresponding values of the tangential shear stress for cavity aspect ratios of 1.0 and 0.5 and a bulk flow velocity of 5.00 cm/s. It is understood that the derivative $d\sigma/dx^*$ depends on bulk flow velocity and cavity geometry. However, it is more convenient to study the interrelationship between $d\sigma/dx^*$, the interface velocity, and the cavity length by selecting a value for $d\sigma/dx^*$ rather than by determining it. For a given value of $d\sigma/dx^*$, the interface velocity is seen to increase with increasing cavity length. Examination of the stress values for various interface tension gradients indicates that the stresses at the cavity side of the interface decrease, while those on the channel side increase for increasing $d\sigma/dx^*$. The implication here, is that, as the cavity aspect ratio increases, the interface becomes more mobile. This agrees with observations of rising or falling drops in liquid–liquid two-phase systems, in

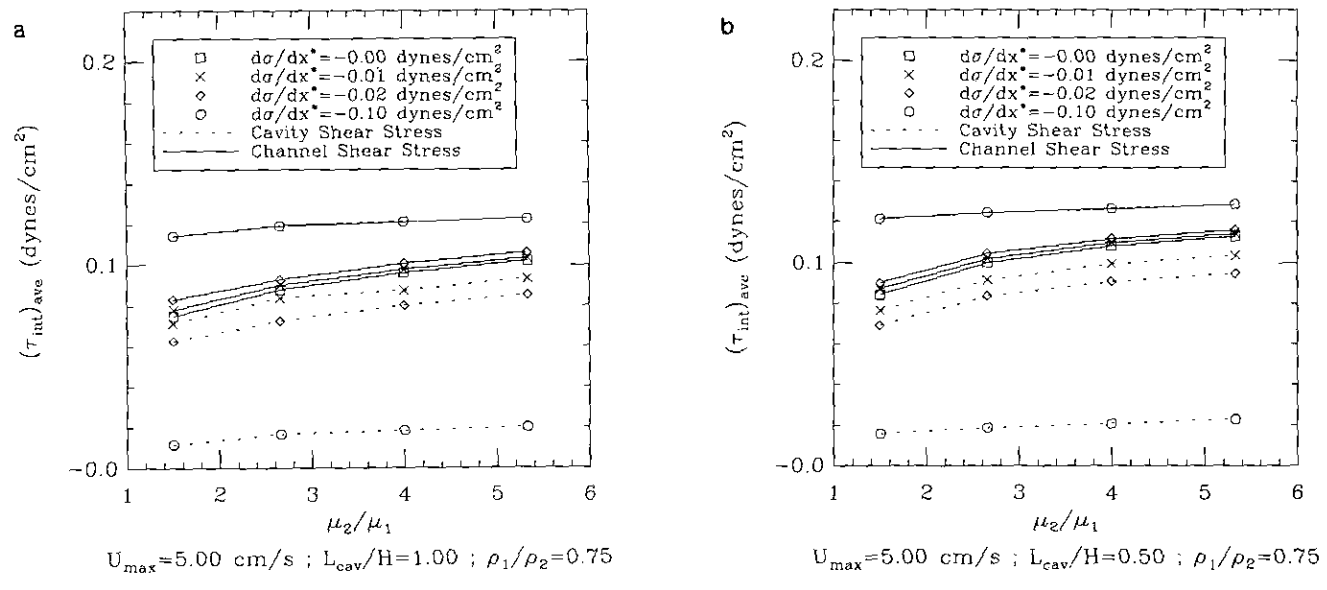

FIG. 13. Interface shear stress versus viscosity ratio.

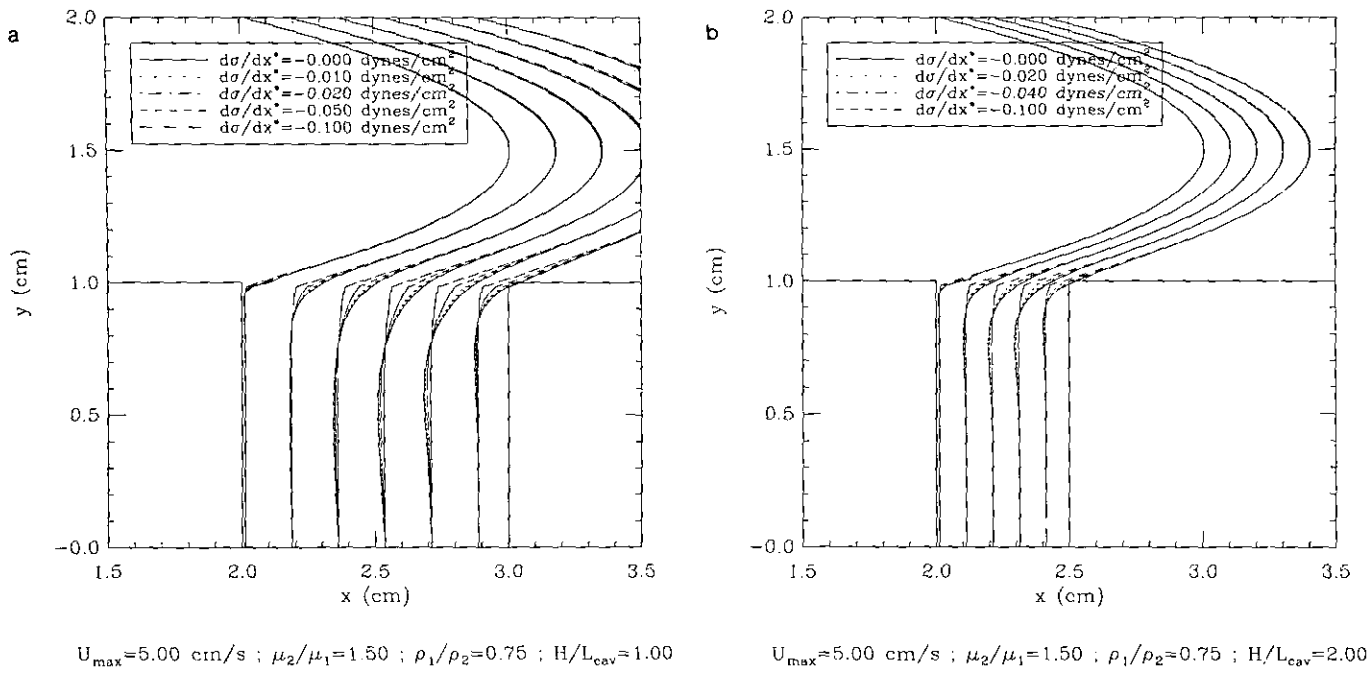

FIG. 14. Normalized velocity profiles for various interfacial tension gradients.

that, as the terminal velocity or the diameter of the drop increases, the drop surface exhibits increasing mobility. In addition, it is seen that a slight variation in the surface tension coefficient decreases the mobility of the interface significantly. In all cases, the interface velocity is seen to decrease with increasing μ_2/μ_1 as would be expected, since for increasing values of μ_2, the interface more nearly resembles that of a solid boundary. Likewise, the stress at the channel side increases as the interface becomes more rigid. At the cavity side, the viscous shear rate decreases with increasing viscosity ratios.

Experimental and numerical studies [24, 25] have shown that for drops of large diameter, the surface exhibits a higher degree of mobility and internal circulation, indicating larger values of shear stress at the inside drop surface. In addition, smaller drops exhibit terminal velocities identical to those of

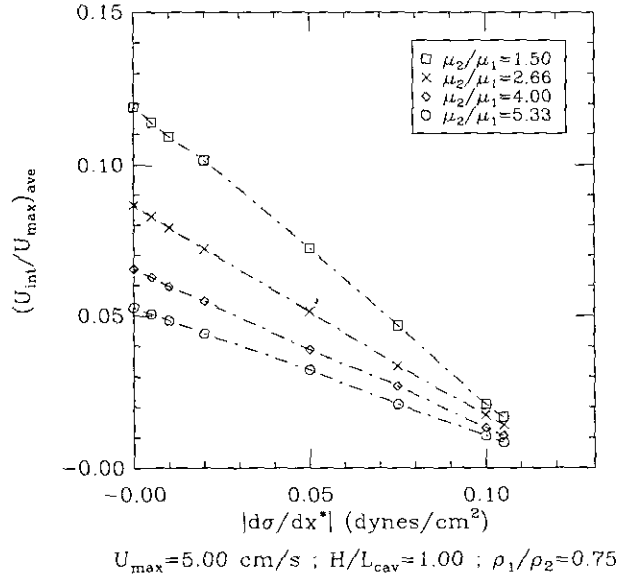

FIG. 15. Normalized interface velocity versus interface tension gradient.

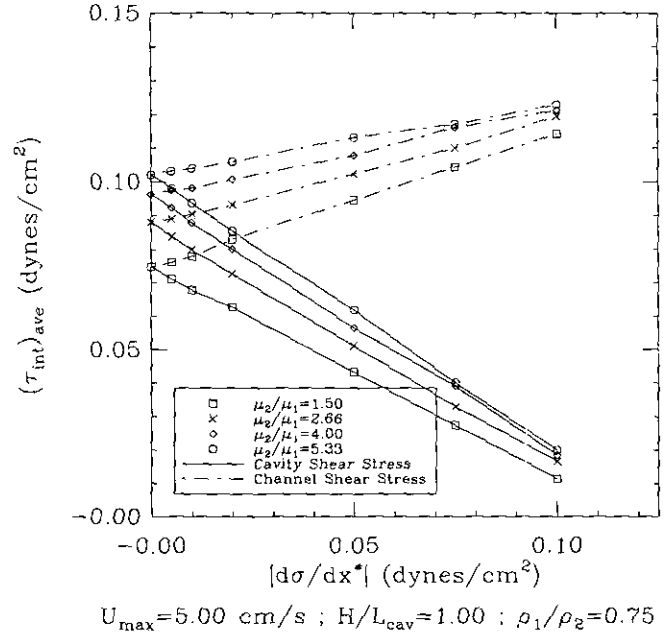

FIG. 16. Interface shear stress versus interface tension gradient.

rigid spheres of the same size and density and lesser values for larger drops with higher surface mobility. Likewise, the stress at the outer surface of the drop decreases for increasing diameters, resulting in the observed higher terminal velocities. In the velocity profiles plotted in Fig. 14, this variation of the tangential stresses is evidenced by the departure of the velocity in the channel above the cavity from the familiar parabolic profile of Poiseuille flow.

A basic assumption of this study is that of a linear variation of the interface tension coefficient. While no mention has been made about the mechanism causing this variation, it is known that the interface tension is dependent upon both the temperature and composition of the two-phase system under consideration. For drops translating through fluid media, the tendency for surfactants to accumulate at the interface, and subsequently be swept to the aft portion of the drop surface, produces a positive concentration gradient, resulting in a decrease in surface tension. A similar situation exists in cases involving heat transfer to or from drops in direct-contact heat exchangers. A drop of cold oil translating through a hot fluid in a heat exchange column develops the highest temperature gradients at the downstream portion of the drop surface, resulting in lower values of surface tension. In addition, experimental observations indicate that, in both cases internal fluid circulation inside the drops is suppressed due to the rigid behavior of the drop surface. Thus, an increase in the concentration of surfactant or temperature gradients is accompanied by a reduction in interfacial tension coefficients and a corresponding decrease in mobility of the interface.

Figures 15 and 16 illustrate the effects of a negative interfacial tension gradient on the flow in a liquid–liquid driven cavity. Consistent with the above observations, the interface velocity is seen to decrease with decreasing surface tension. The influence of the viscosity ratio is also displayed. Figure 14 also shows the effects of various values of $d\sigma/dx^*$ on the overall flow field. As expected, for increasing magnitude of $d\sigma/dx^*$, the circulation within the cavity weakens, as the interface velocity, as well as the shear stress at the cavity side of the interface, decreases.

Essentially, the parametric study shows that the liquid–liquid driven cavity flow exhibits a behavior which is very similar to the behavior of drops translating in a second, immiscible liquid. Depending on geometry and on the variation of interface tension in flow direction, the liquid–liquid interface will be rigid, partially mobile, or, in rare cases, fully mobile.

CONCLUSION

Liquid–liquid driven cavity flow was studied numerically. Assumptions made with regard to the behavior of the liquid–liquid interface were based on experimental evidence. The behavior of liquid–liquid driven cavity flow is shown to be very similar to that of liquid drops translating in a second immiscible liquid.

REFERENCES

1. U. Ghia, K. N. Ghia, and C. T. Shin, *J. Comput. Phys.* **48**, 387 (1982).
2. K. N. Ghia, W. L. Hankey, and J. K. Hodge, *AIAA J.* **17** (3), 298 (1979).
3. A. S. Benjamin and V. E. Denny, *J. Comput. Phys.* **33**, 340 (1979).
4. R. Schreiber and H. B. Keller, *J. Comput. Phys.* **49**, 310 (1983).
5. S. G. Rubin and P. K. Khosla, *Int. J. Comput. Fluids* **9**, 163 (1981).
6. L. E. Scriven, *Chem. Eng. Sc.* **12**, 98 (1960).
7. J. F. Harper and D. W. Moore, *J. Fluid Mech.* **32**, 367 (1968).
8. A. Frumkin and G. Levich, *Zh. Fiz. Khim.* **21**, 1183 (1947).
9. G. Levich, *Physiochemical Hydrodynamics* (Prentice-Hall, New York, 1972).
10. P. Savic, Ref. No. MT-22, Natl. Res. Council Can. Div. Mech. Engng., 1953 (unpublished).
11. R. M. Griffith, *Chem. Eng. Sci.* **12** 198 (1960).
12. R. E. Davis and A. Acrivos, *Chem. Eng. Sci.* **21**, 681 (1961).
13. B. Levich, *Phys. Chem. Hydrodyn.* **2**, 85, 95 (1981).
14. R. Clift, J. R. Grace, and M. E. Weber, *Bubbles, Drops, and Particles* (Academic Press, New York, 1978).
15. J. Walter and E. Marschall, UCSB-ME-89-71, 1989 (unpublished).
16. G. R. Johnson, E. Marschall, and J. H. Esdorn, *Rev. Sci. Instrum.* **56**, 264 (1985).
17. T. McWaid and E. Marschall, *Exp. Thermal Fluid Sci.* **232** (1990).
18. H. T. Davis and L. E. Scriven, *Adv. Chem. Phys.* **49**, 357 (1981).
19. C. W. Hirt and B. D. Nicholas, *J. Comput. Phys.* **34**, 390 (1980).
20. C. W. Hirt and B. D. Nichols, *J. Comput. Phys.* **39**, 203 (1981).
21. G. E. Mansell, Ph.D. dissertation, University of California, Santa Barbara, 1990.
22. J. E. Welch, F. H. Harlow, J. P. Shannon, and B. J. Daly, Los Alamos Scientific Laboratory Report, LA-3425, March 1966 (unpublished).
23. B. J. Daly, *J. Comput. Phys.* **4**, 97 (1969).
24. J. F. Hutchins, Ph.D. dissertation, University of California, Santa Barbara, 1988 (unpublished).